

Catalysts by pyrolysis: Direct observation of transformations during re-pyrolysis of transition metal-nitrogen-carbon materials leading to state-of-the-art platinum group metal-free electrocatalyst

Yechuan Chen ^{1a†}, Ying Huang ^{1b†}, Mingjie Xu ², Tristan Asset ^{1a}, Xingxu Yan ^{2a},
Kateryna Artyushkova ³, Mounika Kodali ^{1a}, Eamonn Murphy ^{1a}, Alvin Ly ^{1b}, Xiaoqing Pan ^{2a,b},
Iryna Zenyuk ^{1a,b***}, Plamen Atanassov ^{1a*}

¹ National Fuel Cell Research Center, University of California Irvine, California 92697, USA

a. Department of Chemical & Biomolecular Engineering, University of California Irvine, California 92697, USA

b. Department of Materials Science & Engineering, University of California Irvine, California 92697, USA

² Irvine Materials Research Institute, University of California Irvine, California 92697, USA

a. Department of Materials Science & Engineering, University of California Irvine, California 92697, USA

b. Department of Physics and Astronomy, University of California Irvine, California 92697, USA

³ Physical Electronics, Chanhassen, Minnesota 55317, USA

* Corresponding author. Email address: plamen.atanassov@uci.edu

** Co-corresponding author. Email address: iryna.zenyuk@uci.edu

† The authors contributed equally

Abstract

Transition metal-nitrogen-carbon (M-N-C) materials have been the focus of scientists' efforts to address the rising need for earth-abundant materials solutions for energy technology and decarbonization of the economy. They are viewed as one of the most promising candidates to replace platinum group metal (PGM) catalysts in the fuel cell and energy conversion fields, including the application of oxygen reduction reaction, carbon dioxide reduction reaction, and nitrogen reduction reaction. In the effort to improve M-N-C materials properties and achieve atomic dispersity of the transition metal in the carbonaceous matrix, a re-pyrolysis process has been proposed. This secondary heat treatment process of already obtained primary pyrolysis-derived M-N-C materials has been widely reported to substantially improve the electrochemical performance and operational stability of the catalysts. Here, we report a systematic investigation of this process used on samples of templated M-N-C catalysts to obtain state-of-the-art catalysts via *in situ* heating X-ray photoelectron spectroscopy (XPS), scanning transmission electron microscopy (STEM), energy-dispersive X-ray spectroscopy (EDS), electron energy loss spectroscopy (EELS), X-ray diffraction (XRD), and X-ray computed tomography (CT) characterization methods. It is found that the re-pyrolysis of M-N-C materials could result in the partial amorphization of the carbonaceous substrate. It causes the rearrangement and transformation of multitudinous N moieties, leading to optimization of their morphological display and association with atomically dispersed transition metal dopants. Ultimately, the re-

pyrolysis results in an increase in uniformity of the active Fe-N_x sites distribution without the formation of nano-crystalline phases (metallic or carbide) and with overall preservation of the morphology of the carbonaceous framework achieved during the first formative pyrolysis step of the templated synthesis. These observations provide confirmation that empirically established re-pyrolysis is recommended to be used on all M-N-C materials despite the different synthesis routes to obtain a practical advanced catalytic material.

Introduction

With the increasing demand for environmentally friendly power sources, the electrochemical catalysts have attracted tremendous research interests in recent years for the applications of fuel cells and energy conversion[1]. Among numerous materials suggested, the transition metal-nitrogen-carbon (M-N-C) electrocatalyst is one of the most promising candidates to replace platinum group metal (PGM) catalysts addressing the cost and availability issues and demonstrating a trajectory in performance and durability improvement[2]. These materials have been historically inspired by the oxygen-binding heme structure in hemoglobin[3], and have a long record of efforts on their synthesis and integration for practical applications. Most notably these materials have been reported as reasonable alternatives to the conventional PGM catalysts for oxygen reduction reaction in a fuel cell cathode[4]. Recently this category of electrocatalysts has also been introduced[5] to the area of carbon dioxide reduction reaction[6,7]. Moreover, some attempts[8-10] of utilizing M-N-C electrocatalysts have even been made for the extremely difficult nitrogen reduction reaction under ambient conditions. Considering the versatility of M-N-C materials in electrochemistry, it is essential to fully understand their synthesis, structure, and catalysis mechanism in order to rationally improve their performance and stability. These materials display a set of chemically close M-N_x ($x=2-4$) active sites, as well as the multitudinous N moieties that participate in the electrocatalysis of oxygen reduction reaction (ORR) [11]. Structure-to-property relationships with respect to these various active sites have been researched via spectrum of characterization methods, including X-ray adsorption spectroscopy[12-14] (XANES / EXAFS), X-ray photoelectron spectroscopy[15] (XPS), Mössbauer spectroscopy[16,17], molecular probes[18-20], Raman spectroscopy[21], and correlated to the results obtained by different modeling platforms (*ab initio* and DFT-based) [22-24]. The effect of the metal loading on the active sites' formation [25,26] and the durability of this class of materials [27,28] were also investigated. However, the synthesis and modification of M-N-C catalysts still lack comprehensive understanding and was nominally regarded as a “black box”, despite being used universally. Most

reported approaches require pyrolysis to form N-doped carbon and M-N_x sites using different precursors. The high temperature, as well as specific atmosphere, prevent the utilization of most characterization methods. Recently, Li *et al.*[14] reported the continuous observation of Fe-N_x formation via *in situ* heating XAS, becoming the first to get insight into the pyrolysis process rather than tuning precursors and conditions. In our most recent study, we have demonstrated the first direct observation of pyrolytic synthesis of M-N-C catalysts, obtained by sacrificial support method (a hard template technique) by a set of *in situ* techniques[29]. This study demonstrated morphological evolution of the carbonaceous matrix and subsequent chemical transformation of the nitrogen moieties incorporating in the matrix and evolving continuously across the temperature-time trajectory. We established that the pyrolysis process has three distinct stages: (i) thermal ramp responsible for the macroscopic morphology transformation and “shaping” of the material; (ii) carbonization, formation of amorphous carbon domains and emergence of metallic nanoparticles; (iii) graphitization of the carbonaceous matrix combined with the evolution of atomically dispersed metal moieties associated with the nitrogen ones to form the M-N_x active sites. All three stages are needed to form the catalytically active material, however moieties compromising the catalyst’s activity and selectivity and detrimental to catalyst durability also appear in the resulting matrix. HF etching, primarily used for removing the hard template material (amorphous silica particles used in the process of the carbonaceous matrix formation), additionally removes some of these moieties, notably the metallic nanoparticles, transition metal carbides and oxides, and other surface impurities. However, it cannot remove the structurally embedded metallic or carbide particles, which compromises the “purity” of atomically dispersed transition metal type sites.

The desire to have explicitly atomically dispersed M-N-C catalysts led scientists to attempt a second pyrolysis step. Dual pyrolysis or subsequent two-step pyrolysis methods have been briefly mentioned in previous publications[30-34], without additional explanation or specific attention. The “re-pyrolysis” unexpectedly resulted in a much greater positive impact on the overall catalyst performance, allowing the initial activity to be sustained, alleviating some of the degradation modes, and generally improving the durability.[35] Re-pyrolysis, as a materials synthesis method addition, is a way of substantially improving the performance of numerous M-N-C catalysts that performed “below expectations” after the first pyrolysis. This process is less sensitive to variables and can be easily scaled for industrial applications.

This paper addresses the issues of re-pyrolysis in detail through a plethora of *in situ* techniques. Here, we report observational results as we directly monitor the continuous changes of the M-N-C catalyst during the re-pyrolysis process via several *in situ* heating spectroscopy/microscopy

characterization methods: XPS, STEM, EDS, EELS, XRD and X-ray CT. The catalyst tested was a non-specific iron-nitrogen-carbon material that has been constantly researched and reported for several years, which allow for generalized results for revealing the function of the re-pyrolysis.

Results

The advantage of re-pyrolysis of M-N-C catalysts to the electrocatalytic performance has been partially studied and reported by our group previously[35]. By testing initial Fe-N-C catalysts and re-pyrolyzed Fe-N-C catalysts under NH_3 in both acid and alkaline media via linear sweep voltammetry on rotating ring disk electrode, it was found that the re-pyrolysis process under ammonia increased the diffusion current density and decreased the peroxide yield but did not change the half-wave potential. Improved performances in both media was expected to be as a result of the removal of surface oxides and residual iron nanoparticles and the formation of a beneficial chemical composition with a large amount of aliphatic and graphitic carbon and nitrogen, particularly in the iron coordinated environment and the pyridinic nitrogen. The previous study was done *ex situ*, where the chemistry of the material was characterized after each step of the synthesis, including the re-pyrolysis. In-situ chemical observation during the re-pyrolysis step avoids the contamination of air exposure to the surface chemistry. Here, a set of electrochemical RRDE data tested with freshly synthesized Fe-N-C catalysts via the same recipe is given in **Figure 1**, showing improvement with re-pyrolysis.

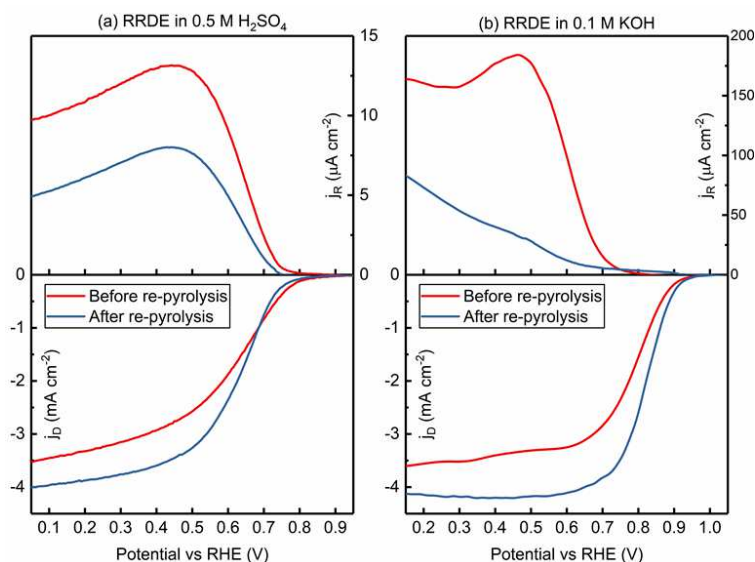


Figure 1. The polarization data of Fe-N-C materials before and after re-pyrolysis in (a) 0.5 M sulfuric acid and (b) 0.1 M KOH respectively. Both were tested on RRDE with 1600 rpm rotation speed and 5 mV s^{-1} scanning rate.

Figure 2 follows the changes in Fe-N-C chemistry by *in situ* XPS with heating under ultra-high vacuum conditions. A low energy survey spectra including the binding energy region captures all of the relevant XPS transitions - iron (Fe 2p around 710 eV), fluorine (F 1s around 686 eV), oxygen (O 1s around 532 eV), nitrogen (N 1s around 399 eV) and carbon (C 1s around 284 eV) - between 850 eV to 250 eV. The completed binding energy range survey spectra are presented in **Figure S1**. F 1s peak originates from the use of hydrofluoric acid to etch silicon dioxide during synthesis. Some HF molecules may remain trapped in pores even after rigorous washing to a neutral pH and drying at low temperature (80 °C to 150 °C in conventional lab ovens). Comparing the results of the initial 150 °C and the final 150 °C, it was found that, after heating, surface concentration of O 1s and F 1s decreased from $5.73 \pm 0.15 \%$ to $2.55 \pm 0.18 \%$ and from $0.62 \pm 0.07 \%$ to $0.09 \pm 0.09 \%$ respectively. Considering the minimum detection limit of XPS of 0.1 at% [36], it can be concluded that the fluorine disappears after heating. The decrease in the amount of oxygen may be due to the removal of pre-adsorbed molecules as well as changes in the carbon chemistry. The latter was observed in the previous study where the amount of surface oxides decreased after re-pyrolysis [35]. The removal of pre-adsorbed species can be implied from the decrease in the intensity of the peak corresponding to the O 1s region (binding energy larger than 535 eV) as shown in **Figure S4(k)**, corresponding to physically adsorbed water [37] and carbon dioxide [38]. **Figure 2(c)** also indicates that the surface concentration of Fe did not change during re-pyrolysis, with the same initial and final atomic percentages of 0.33%. This suggests that iron distribution between the surface (sampling depth for Fe 2p is ~ 4.5 nm [39]) and deeper layers were not affected during the re-pyrolysis. This indicates that there was no noticeable transfer of iron between the material surface (calculated as ~ 4.5 nm, three times of inelastic mean free path [39]) or within. Because the surface “cleaning” occurs through desorption of adsorbed gas and removal of surface oxides, the C at% increased from $89.8 \pm 0.3 \%$ at room temperature to $93.9 \pm 0.4 \%$ after cooling down to 150 °C after re-pyrolysis. The change in the amount of nitrogen can be estimated from the surface concentration of N and N / C ratio. N amount was recorded at ~ 3.5 at% initially, then increased to a maximum of $\sim 3.8 \%$ during re-pyrolysis at around 550 °C, and decreased to $\sim 3.3\%$ after the sample had cooled down to 150 °C. N/C ratio reaches a maximum between 450-650 °C. This observation will be further discussed in an interpretation of the chemistry of nitrogen from high-resolution N 1s spectra.

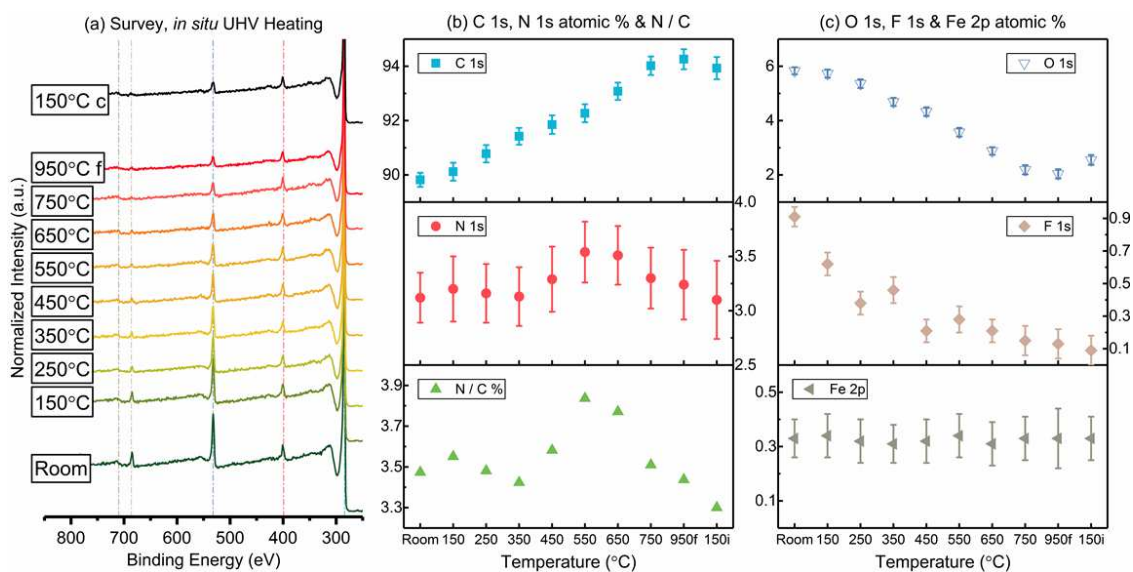


Figure 2. Survey XPS of Fe-N-C catalyst *in situ* heating in ultra-high vacuum condition. (a) Survey spectra ranging from 850 eV to 250 eV. (b) Element composition results of C and N, in addition to the calculated ratio of N / C. (c) Element composition results of O, F and Fe. The term “950 °C f” refers to “flash”, unrestricted ramping rate from 750 °C to 950 °C without holding. The term “150 °C c” refers to “cool”, holding at 150 °C for test after natural cooling. The 5 vertical lines in (a) refer to Fe 2p, F 1s, O 1s, N 1s and C 1s from left to right respectively.

The changes in high-resolution C 1s during *in situ* UHV heating are shown in **Figure 3**, while all C 1s spectra curve fittings are shown in **Figure S2**. The atomic concentrations of each C chemical state are listed in **Figure S5**, based on the corrected calculation of total C atomic concentration at every temperature point. The zoomed-in lowest binding energy region of overlapped spectra in **Figure S2(k)** shows a continuous binding energy shift to higher values with increasing temperature. To compare spectra during heating and after cooling to the initial spectrum, the difference spectra were obtained by normalizing the spectra to the same area and subtracting the initial spectrum from the subsequent as shown in **Figure 3(c)**. From a comparison of the C 1s spectra at initial room temperature, 150 °C before re-pyrolysis, and 150 °C after cooling in **Figure 3(c)**, a positive 0.2 eV shift of maximum peak from 284.5 eV to 284.7 eV can be seen. This shift and the corresponding difference plot can be further divided into two binding energy regions of change in carbon chemistry. The first is the decrease of peaks around 284.5-284.7 eV and an accompanying increase in the peak around 285-285.5 eV. This change is due to the rearrangement of the carbonaceous framework, as the graphitic carbon[40,41] (*i.e.* sp^2 hybridization) signal at 284.5 eV decreased while the amorphous carbon[41,42] (*i.e.* sp^3 hybridization) signal at 284.8 eV or higher increased. Also, as **Figure 3(e)** shows, the total amount of sp^2 and sp^3 carbon did not change significantly during re-pyrolysis ($\sim 60.2\%$ and $\sim 57.8\%$ for initial 150 °C and final 150 °C, respectively). Hence, the re-pyrolysis process converted graphitic C (decrease from $39.4 \pm 3.7\%$ to $14.7 \pm 3.5\%$) into the amorphous state (an increase from $21.0 \pm 4.0\%$ to $43.1 \pm 4.3\%$),

resulting in a more porous carbonaceous material structure. This facilitates the mass transport of ions and molecules during the reaction, due to increasing diffusion current density which was described in **Figure 1** previously. A minor effect is the slight increase of the intensity of C 1s of the region within 286 eV binding energy, the position where C-N contributes, from $13.9 \pm 1.3 \%$ for the initial 150 °C sampling to $14.9 \pm 2.0 \%$ for the final 150 °C sampling. From changes in the amount of elemental oxygen, we have speculated that during re-pyrolysis, surface carbon oxides were being removed from the surface. Concomitantly, the amount of carbon-oxygen species does not change, as **Figure 3(f)** shows.

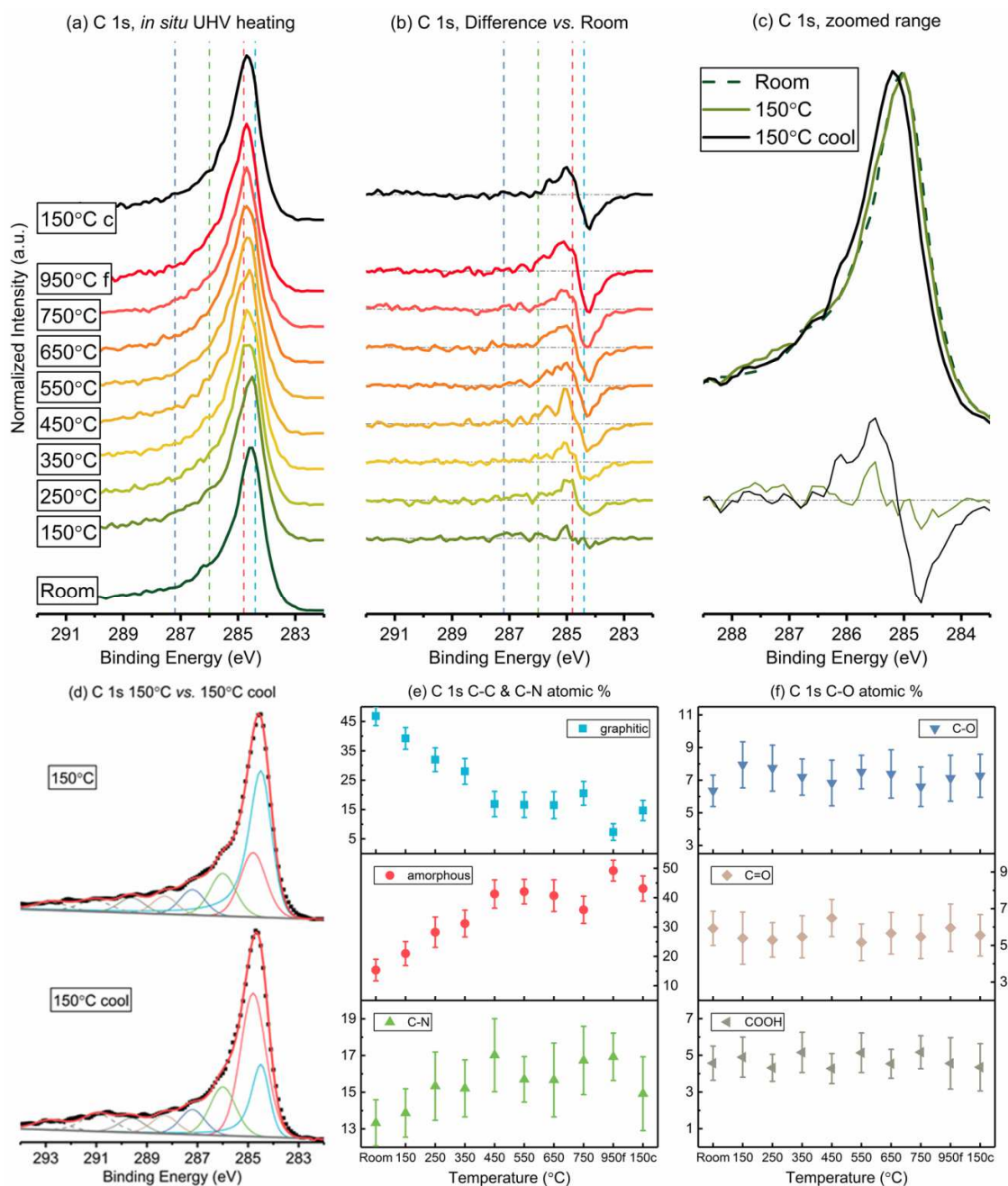


Figure 3. C 1s XPS of *in situ* UHV heating Fe-N-C catalyst. (a) C 1s spectra measured while holding at every 100 °C. (b) Difference plots of spectra *versus* the one measured at room temperature (c) C 1s spectra in zoomed range from binding energy of 288.5 eV to 283.5 eV. (d) Curve fit plots of 150°C and 150°C-cool. (e) Fitting results of graphitic C, amorphous C and C-N. (f) Fitting results of C-O, C=O and COOH.

The changes in high-resolution N 1s during *in situ* UHV heating are shown in **Figure 4**, with N 1s spectra curve fittings shown in **Figure S3**. The atomic concentrations of each N moiety is listed in **Figure S5**, based on the corrected calculation of total N atomic concentration at every temperature point. Upon heating to ~450°C there is no change in nitrogen chemistry. At ~450°C,

regions around 397.5 eV and around 399.7 eV start experiencing a decrease in intensity. According to our previously reported density functional theory calculation results[22,23,41,43] and other reported N 1s results[44-46], the smaller binding energy range change is due to the removal of edge pyridinic N and unstable imine N, and the second region is where a decrease of hydrogenated N-H (including pyrrolic N and hydrogenated pyridinic N) would contribute to. The curve fit results shown in **Figure 4(d)(e)(f)** provide quantitative insight into changes in N chemistry. It can be found that after re-pyrolysis, the amount of pyridinic N decreases slightly from $19.1 \pm 4.9 \%$ to $15.0 \pm 4.5 \%$ while the amount of metal-N_x increases from $10.9 \pm 4.1 \%$ to $16.6 \pm 5.7 \%$, with a high standard deviation indicating a heterogeneous composition. The amount of surface N-H decreases significantly from $41.5 \pm 6.1 \%$ to $32.7 \pm 8.1 \%$ while the amount of graphitic N increases from $8.3 \pm 4.4 \%$ to $21.2 \pm 6.6 \%$. Moreover, bulk N-H which has a much higher core level shift[22,23] around 402.8 eV also has the most significant decrease from $11.6 \pm 4.6 \%$ to $3.3 \pm 3.0 \%$. In conclusion, the re-pyrolysis process gave a more balanced nitrogen-carbon structure: a small reduction in edge pyridinic nitrogen sites prone to protonation and hydrogenation, stabilization of metal-N, a dramatic decrease in both surface and bulk hydrogenated sites N-H, and a higher amount of graphitic N. Small amounts of hydrogenated N should result in a more selective ORR mechanism with a smaller amount of nitrogen atoms contributing to the peroxide yielding reaction. Coincidentally, an increase in graphitic N will improve the surface ionic conductivity and increase the diffusion current density[47], as described in **Figure 1** previously.

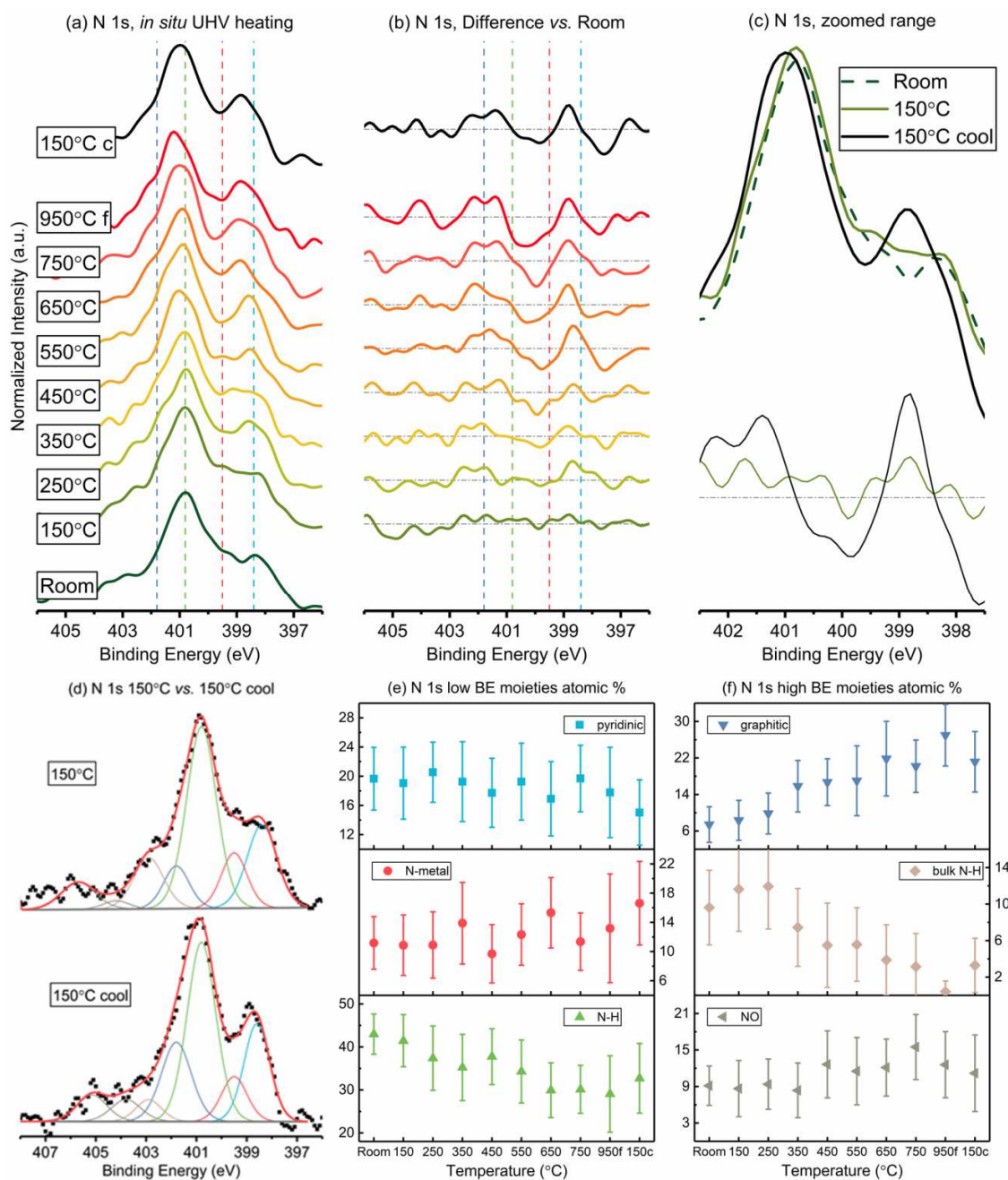


Figure 4. N 1s XPS of *in situ* UHV heating Fe-N-C catalyst. (a) N 1s spectra measured while holding at every 100 °C. (b) Difference plots of spectra *versus* the one measured at room temperature. (c) N 1s spectra in zoomed range from binding energy of 402.5 eV to 397.5 eV. (d) Curve fit plots of 150 °C and 150 °C-cool. (e) Fitting results of pyridinic N, N-metal and N-H. (f) Fitting results of graphitic N, bulk N-H and NO.

To help explain the changes of X-ray photoelectron spectra during re-pyrolysis, *in situ* UHV heating STEM experiments were performed and displayed in **Figure 5** for two different regions. For the cluster / single atom region shown in **Figure 5(a)** with the corresponding enlarged photos

in **Figure S6**, there is a bright area in the center portion of the top row which could be a small agglomeration of iron atoms. With the temperature increasing, this agglomeration continuously disintegrates and it diffuses into the carbonaceous structure, becoming smaller clusters or single atoms (easily recognized in the enlarged images). The diffusion rate becomes quite fast at 950 °C. During the natural cooling progress to room temperature, these diffused iron atoms did not re-agglomerate but remained dispersed. Moreover, from the bottom row, which shows the zoomed-in region, it can be found that the diffusion occurred not only on the surface but also within the carbonaceous matrix, explaining why there was no apparent change of Fe atomic percentage during re-pyrolysis in XPS survey spectra as **Figure 2(a)** shows. After re-pyrolysis, some Fe clusters stayed hexagonal or cubic shape. It is still unknown whether these clusters are bonded with neighboring C / N atoms or not. However, this series of STEM images could explain why the graphite C concentration decreases while the amorphous C concentration increases after re-pyrolysis, as well as the decreasing amounts of Fe-N₄ moieties.

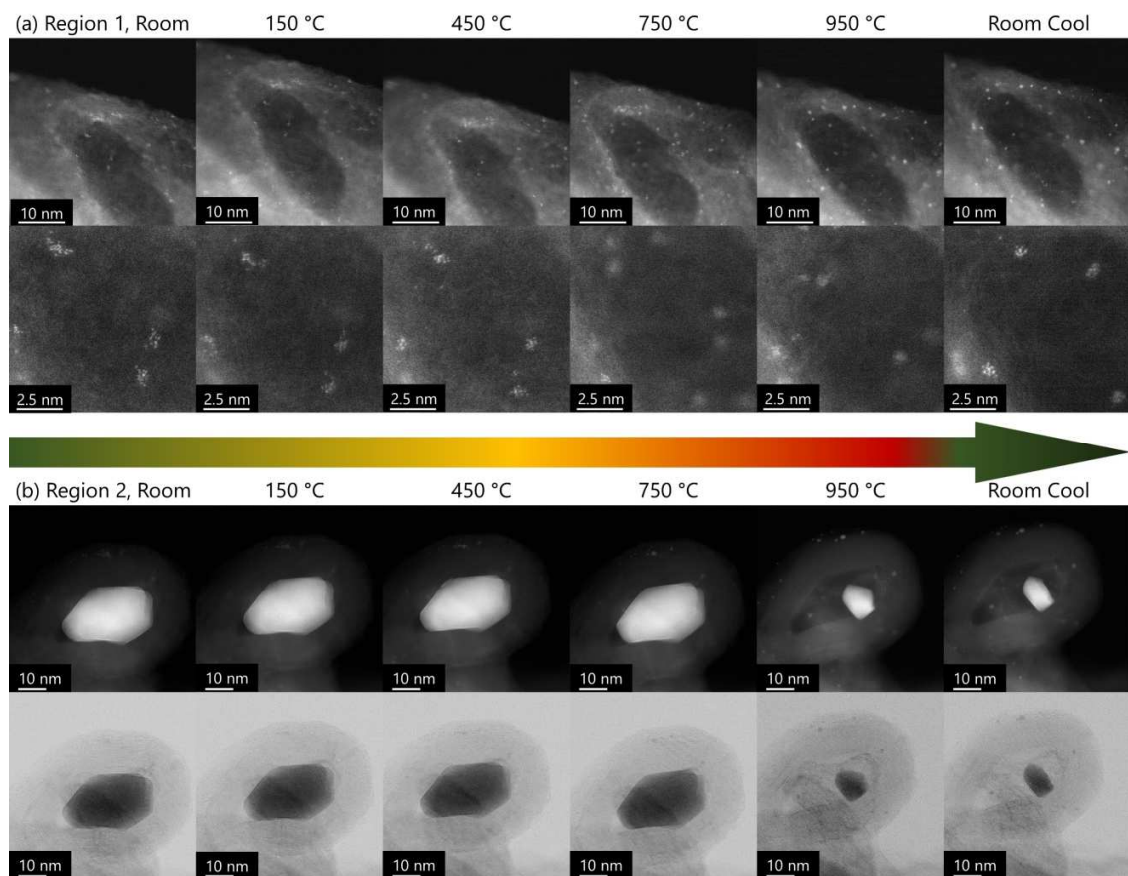


Figure 5. STEM photos of *in situ* UHV heating Fe-N-C catalysts. (a) The cluster / single atom region. The bottom row is the zoomed-in dark center part of the top row. Enlarged photos for Room and Room Cool can be found in **Figure S5**. (b) The nanoparticle/carbide region. The bottom row is the corresponding bright field version of the top row. Enlarged photos for Room and Room Cool can be found in **Figure S6**.

Another interesting finding from STEM imaging is the nanoparticle/carbide region and is shown in **Figure 5(b)**, with the enlarged photos in **Figure S7**. A 30 nm size nanoparticle consisting of iron and , most likely carbon as well, could be found in the center of the photos surrounded by a thick layer of graphite (where the lattice can be recognized in the enlarged photos), which may explain why it was not etched by the acid during the synthesis. This kind of nanoparticle existence in M-N-C catalysts has been reported by several research groups (*e.g.* Wu *et al.* & Chung *et al.*[48,49] of Los Alamos National Lab, Wu *et al.*[50] of University at Buffalo, Strickland *et al.*[31] of Northeastern University, Li *et al.*[51] of University of Montpellier and Möller *et al.*[52] of TU Berlin) even with the use of different synthesis precursors and pyrolysis parameters. Similarly to **Figure 5(a)**, the continuous diffusion of iron atoms to form a small cluster and single atom during the re-pyrolysis is observed. To compare, the nanoparticle also has a similar diffusion progress, but the obvious decrease occurs only at 950 °C. After heating, this large nanoparticle decreases in size to 10nm. The area of the particle was 27 times smaller than that at the initial state, releasing vast amounts of iron atoms back into the carbonaceous structure. The fresh Fe could transform into either iron clusters or single atom sites, but most likely Fe-N₂ sites according to the change of N 1s XPS described previously.

To investigate how nitrogen distributes with iron during the re-pyrolysis, low-voltage STEM imaging and simultaneous electron energy loss spectroscopy (EELS) was done to observe the transformation during the *in situ* re-pyrolysis process. The transformation of an iron cluster-rich area was shown in **Figure 6**, with the bright scattered spots in the STEM images showing the iron atoms diffused over the carbonaceous matrix surface when the temperature was elevated. However, from the comparison among different EELS elemental mappings, it can be found that all C, N, and Fe elements were uniformly distributed in this area before the re-pyrolysis as shown in **Figure 6a** and did not present obvious changes during the process. The overlaid EELS signals of Fe and N further demonstrate that the iron atoms were well surrounded by N during the whole process. Similar findings were observed in different cluster-rich areas (**Figure S9-S11**). The different phenomena of Fe between STEM and EELS results were caused by the limited resolution of EELS mapping (one pixel = 0.33 nm² to 0.44 nm²), but also indicated that the transformation of the iron clusters shown in **Figure 5(a)** is smaller than the EELS resolution. The

calculated correlation between iron and nitrogen also did not show obvious changes on the EELS resolution scale during the re-pyrolysis process (**Figure S12**).

The transformation of an iron particle was also observed during this experiment (**Figure S13**). The particle size was reduced by 55 % (according to the threshold calculation) after undergoing the re-pyrolysis process. Also, the percentage of iron that is correlated with the nitrogen increased 10.1%, indicating that more iron atoms diffused away from the nanoparticle and coordinated with N sites. **Figure S14** shows the zoom-in area near the particles after the sample was re-pyrolyzed. Some uniformly dispersed iron clusters were found on the carbon support, surrounded by nitrogen. Considering the shrinkage of Fe nanoparticles, the newly formed clusters near the nanoparticle most likely arose from the Fe diffusion.

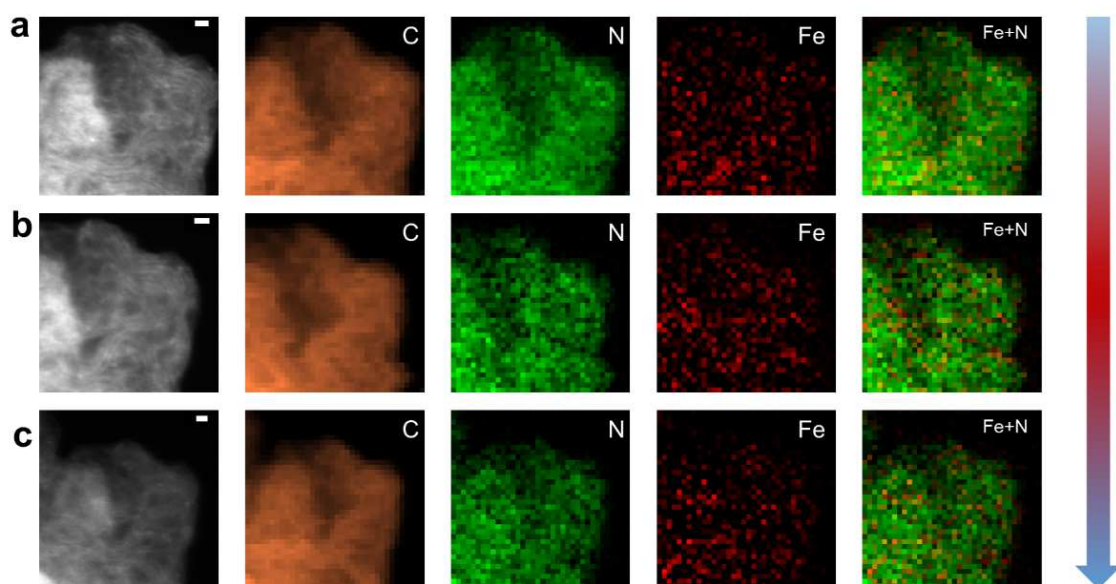


Figure 6. STEM of an iron cluster-rich area (Area I) and the corresponding EELS mapping pictures of *in situ* UHV heating Fe-N-C. (a) the pristine sample. The pixel size is 0.36 nm x 0.36 nm in EELS mapping. (b) sample pyrolyzed to 950 °C. The pixel size is 0.33 nm x 0.33 nm in EELS mapping. (c) sample cold down from 950 °C. The pixel size is 0.33 nm x 0.33 nm – 0.44 nm x 0.44 nm in EELS mapping. Scale bar: 1 nm

To further investigate the diffusion of iron during re-pyrolysis, the energy dispersive X-ray spectra mapping of *in situ* re-pyrolysis was performed in another area with a low magnification due to the limited spatial resolution, as **Figure 7** shows. To avoid electron beam contamination as well as emission interference at high temperatures, EDS mapping imaging was done at the initial

250 °C and final 250 °C for analysis. Most Fe atoms were found to allocate uniformly, behaving like a bright cloud under STEM after the re-pyrolysis. The cracking progress of the pre-existing Fe nanoparticles into atomically dispersed Fe sites is confirmed by the comparison between the 250 °C and 950 °C figures. The EDS mapping indicates that C, N and Fe are homogeneously distributed as Fe-N-C after the re-pyrolysis except for the two 10 nm iron nanoparticles that remained. In addition, the silicon signal of two nanoparticles was also found: one being adjacent to the iron nanoparticles while the other being independent. These were most likely protected by (or incorporated in) the carbonaceous matrix and were not etched by HF during the materials synthesis process. It's surface concentration was too low to be detected in the XPS survey spectra. Moreover, this series of low magnitude STEM figures also indicate that the main carbonaceous structure remained stable during the re-pyrolysis progress, which would be further confirmed by the X-ray computed tomography to be discussed later.

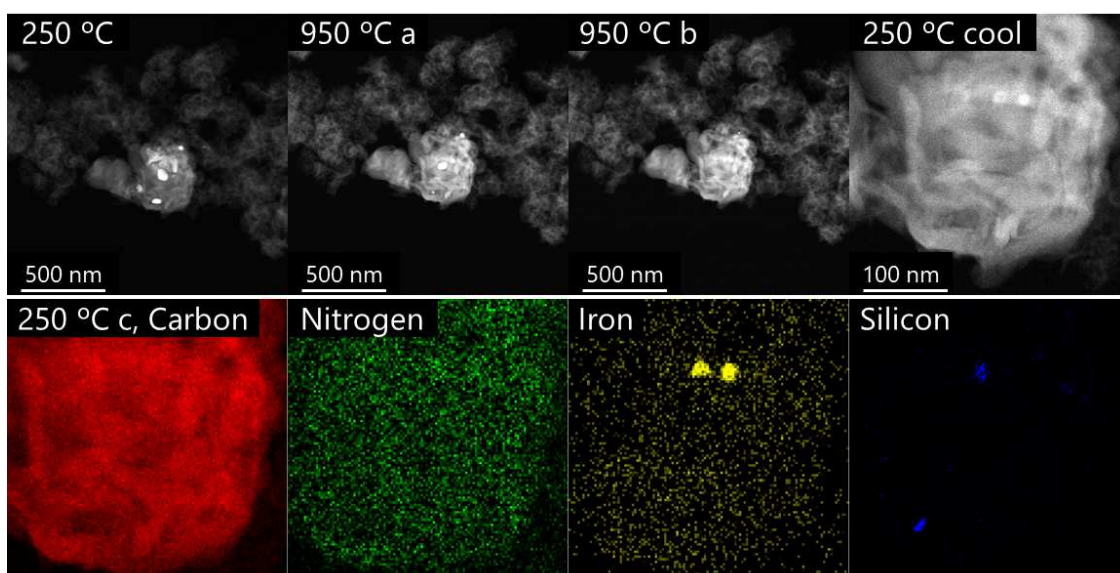


Figure 7. STEM images and corresponding EDS mapping of *in situ* UHV heating Fe-N-C. The top row shows the initial state at 250 °C, the continuous change of nanoparticles at 950 °C and the final 250 °C after cooling down. The bottom row shows the EDS mapping info at 250 °C after cooling down. The term “250 °C c” refers to “250 °C cool”, meaning the test was done after the sample colds down to 250 °C for test.

Considering the apparent nanoparticle transformation during the re-pyrolysis process, *in situ* N₂ heating XRD as well as *ex situ* XRD was performed to check the possible change of crystal structure. The corresponding patterns are displayed in **Figure S15** and **S16** respectively. The signals of AlN, α -Al₂O₃ and graphite were clearly found due to the design of the *in situ* heating setup. The shift of nearly all XRD peaks including the one of Fe-N-C around 26.3° to smaller 2 θ angles during heating was attributed to the thermal expansion of the crystal lattice[53]. The only

exception is the signal around 28° assigned to the (002) of graphite which belongs to the graphite dome. The graphite dome was utilized to protect and isolate the internal high-temperature N_2 and the external cooling air. After excluding the ambient diffraction patterns, it was found that there was neither the appearance of new peaks nor the disappearance of pre-existing peaks during or after the re-pyrolysis, while any changes of 26.3° signal for Fe-N-C was too difficult to estimate due to the peak width. Briefly, *in situ* heating XRD indicates that the re-pyrolysis process does not result in large crystal formation/decomposition for Fe-N-C catalysts.

The possible morphology change during the re-pyrolysis was investigated by *in situ* N_2 heating X-ray computed tomography, as **Figure S17-S18** shows. No significant morphology change (e.g., appearance/disappearance of the pathway, emergence of substantial pores, etc.) was observed during the scanning, although some trivial changes, such as the breaking or formation of small clusters in some areas, happened with the temperature changes. The porosity values in thru-plane direction were calculated in a chosen area (shown as the 3-D structure) of the sample in pristine and final states. The plots of the porosity with the depth in the thru-plane direction show a similar tendency. The porosity increases slightly after the re-pyrolysis process. The difference between the porosity values arises from the image noise difference. The evaporation of the materials in some areas may also contribute to the increase in porosity after the re-pyrolysis. The specific surface area of the pyrolyzed sample and the samples re-pyrolyzed at 450°C , 750°C , and 950°C were calculated with Brunauer–Emmett–Teller (BET) isotherm (Figure S19-S20 and Table S1). All catalysts showed high surface area ($659.7803\text{ m}^2/\text{g}$ - $931.0143\text{ m}^2/\text{g}$) with the isotherms indicating a presence of micropores and mesopores. The number mesopores slightly decreased after re-pyrolysis. Overall, the pore size distributions of all the samples are similar.

To check the stability of the chemical state of M-N-C after re-pyrolysis, a repeated re-pyrolysis was processed and analyzed with *in situ* heating XPS, as **Figure 8** shows. Similarly, different spectra were obtained by the normalization to the same area and the subtraction of the initial spectrum from the final spectrum. The difference spectra between 1st and 2nd re-pyrolysis were also done by subtracting the 1st spectrum from the 2nd one. It can be found that C 1s spectra has no apparent change between 150°C 1st time and 150°C 2nd time, implying that the carbonaceous structure (the M-N-C catalyst “backbone” material) became quite stable after the re-pyrolysis. N 1s spectra also changed, but it can be attributed to a slightly more significant decrease of pyridinic N during the repeated re-pyrolysis. However, the absolute value of this increase was similar to the noises. Hence, this small change could be regarded as negligible, implying that the M-N-C materials becomes stabilized after re-pyrolysis and does not require further heat treatment.

However, considering the XPS facility limitation of the Kratos AXIS Supra which can only continuously stay at 800 °C and instantly go up to 1000 °C (*i.e.* “flash” as described), it is still unknown how the C 1s and N 1s spectra would change after 30 to 60 minutes of holding at 950 °C.

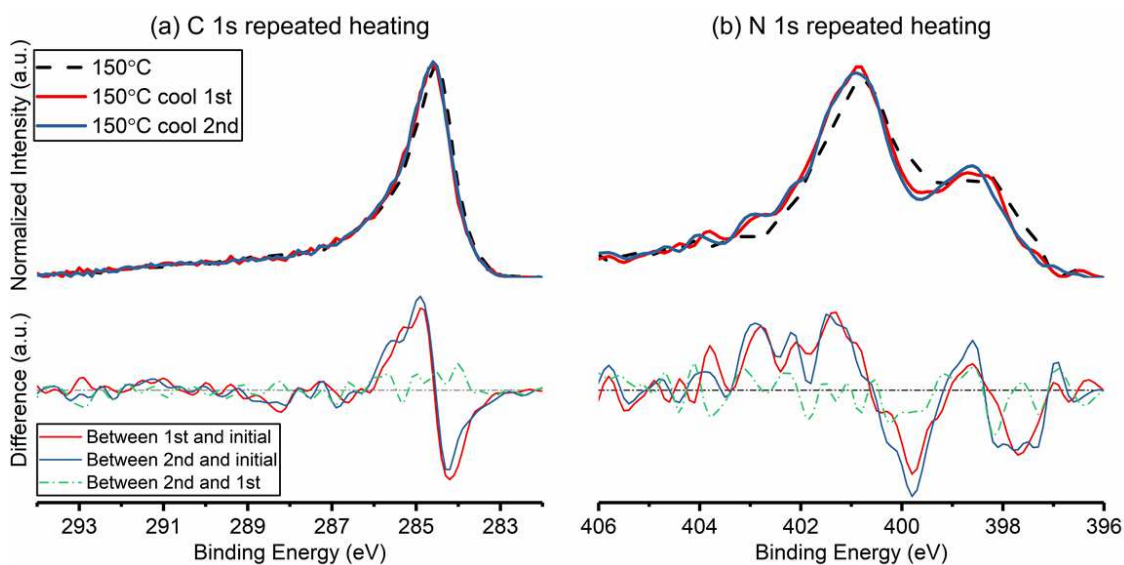


Figure 8. XPS for *in situ* heating and repeated *in situ* heating and the corresponding differences *versus* initial 150 °C. (a) C 1s. (b) N 1s. The repeated heating followed the same ramping and cooling procedure.

The electrochemical performance of the pyrolyzed sample (after HF etching) as well as the samples re-pyrolyzed at 450 °C, 750 °C, and 950 °C was assessed with a rotating ring disk electrode setup (Figure S21). For comparison, the electrochemical performance of Pt/C standard is also provided (Figure S22). The re-pyrolyzed samples show increased half-wave potential and decreased peroxide generation. The improved half-wave potential can be attributed to the increase in the Fe-N_x active site density. The decrease in peroxide yield is due to a more reasonable ratio of N-H (including the pyrrolic N and protonated pyridinic N) and pyridinic N. Moreover, higher capacitance is achieved through re-pyrolysis of the catalyst. This indicates that re-pyrolysis can increase the accessible surface area and decrease the concentration of graphitic carbon.

Conclusion

The combination of several *in situ* UHV / N₂ heating characterization methods performed on a general Fe-N-C material successfully revealed why the re-pyrolysis procedure improves the electrochemical performance of M-N-C materials as well as detailing the chemical and materials synthesis phenomena that occurs during the re-pyrolysis process. (i) The *in situ* XPS indicates

that the re-pyrolysis leads to the complete evaporation of the potentially harmful solvent, a negligible Fe concentration change on the catalyst surface, the amorphization of C, and the rearrangement/optimization of multitudinous N sites. (ii) The *in situ* TEM imaging demonstrates that the re-pyrolysis results in the elimination of undesired Fe nanoparticles, the dispersion (*via* surface diffusion or vapor-phase processes) of Fe atoms, the increase of Fe-N_x sites, and a more uniform distribution of Fe-N_x sites. (iii) The *in situ* STEM-EELS, *in situ* XRD and *in situ* X-ray CT point out that the re-pyrolysis will not cause noticeable crystal phases formation (metallic, oxide or carbide nanoparticles) and does not lead to substantial morphological changes of carbonaceous framework (no new pores, cracks or delamination formation). In addition, our discovery from *in situ* STEM-EDS implies that the impurities present in precursors, which could not be detected by bulk spectroscopies, may cause severe agglomeration of iron during synthesis. Fortunately, it can be reversed by the re-pyrolysis process to a large degree and potentially eliminated. Given the evidence, the process of re-pyrolysis can be classified as a materials purification step of the synthesis procedure.

In summary, the re-pyrolysis provides numerous synthetic advantages and is recommended to be utilized for all metal-nitrogen-carbon (M-N-C) electrocatalysts, no matter the precursors or synthesis parameters. The next stage will be to bring more efforts in investigating how the re-pyrolysis could affect specific commercial carbons and whether it could influence platinum-group-metal electrocatalysts as well.

Methods

Materials Synthesis. The iron-metal-nitrogen catalysts were synthesized via Sacrificial Support Methods[54], using the recipe from the previous publication[7]. A calculated amount of silica, mixed homemade Stöber spheres, LM-150 and OX-50 (Cabot) (1 g, 2.5 g and 2.5 g respectively), were combined with 1.2 g of iron nitrate nonahydrate (Sigma-Aldrich) and 12.5 g of nicarbazin (Sigma-Aldrich) in water to form a viscous solution. After drying and ball-milling, the mixture was pyrolyzed at 975 °C under a 7% H₂-93% N₂ atmosphere. The materials were then etched by hydrofluoric acid (Sigma-Aldrich), washed until the pH reached neutral, dried and ball-milled in sequence to get the pyrolyzed Fe-N-C catalysts. The pyrolyzed Fe-N-C catalysts were then re-pyrolyzed at designated temperatures (450 °C, 750 °C, and 950 °C) under NH₃ for 1h.

The authors noticed that some particles appeared in the pyrolyzed product. It might be due to the inaccurate temperature setting. The particles usually appear when the pyrolysis temperature is

higher than 1000 °C with this precursor. With the accurate pyrolysis temperature, the metal in the product should be atomically dispersed.

Electrochemical Measurements. The electrochemical performances were measured by using a rotating ring disk electrode (RRDE) method. For the data in Figure 1, the catalyst inks with a concentration of $5 \mu\text{g } \mu\text{L}^{-1}$ were prepared by mixing 5 mg of Fe-N-C catalysts, 150 μL of 0.5 wt % Nafion solution (Ion Power) and 850 μL of 4:1 H_2O /Isopropanol (Sigma-Aldrich) under sonication. After dropping a calculated amount of the inks on an RRDE (Pine Research) with a glassy carbon disk of 0.2475 cm^2 area and a platinum ring of 0.1866 cm^2 area, a final electrode layer of 0.175 mg cm^{-2} loading was derived, which is enough to cover the disk surface. Linear sweep voltammetry (LSV) was then performed by using this RRDE as the working electrode, a graphite rod as the counter electrode and a reversible hydrogen electrode (RHE) as the reference electrode, in 0.5 M H_2SO_4 (in house prepared, Sigma-Aldrich) acid media and 0.1 M KOH (in house prepared, BioXtra) alkaline media respectively. The corresponding LSV parameters were set as follows on a WaveNow potentiostat (Pine Research): rotation speed of 1600 rpm, scanning window of 1.1 V to 0 V *versus* RHE in both media for the disk electrode, the potential held at 1.1 V *versus* RHE for the ring electrode, scanning rate of 5 mV s^{-1} . For the data in Figure S20, the catalyst inks with a concentration of $5 \mu\text{g } \mu\text{L}^{-1}$ were prepared by mixing 5 mg of Fe-N-C catalysts, 15 μL of 5 wt. % Nafion solution (Sigma-Aldrich) and 985 μL of 4:1 H_2O /Isopropanol (Sigma-Aldrich) under sonication. A final layer of 0.174 mg cm^{-2} loading was derived. The electrolyte is 0.1 M HClO_4 , and the electrolyte resistance was measured prior to any experiments. The catalyst was activated in a N_2 -saturated electrolyte through 100 cycles at 500 mV s^{-1} between 0.05 and 1.23 V *vs.* RHE, followed by 3 cycles at 20 mV s^{-1} and a linear sweep voltammetry between 0.05 and 1.05 V *vs.* RHE at 20 mV s^{-1} (as a baseline correction). Then, a linear sweep voltammetry between 0.05 and 1.05 V *vs.* RHE at 20 mV s^{-1} was measured at 900 r.p.m at O_2 -saturated electrolyte. The data was corrected from the ohmic losses in solution and the baseline obtained in N_2 -saturated electrolyte.

X-ray Photoelectron Spectroscopy Characterization. High resolution XPS was performed on a Kratos AXIS Supra spectrometer with a monochromatic Al $K\alpha$ source. The catalyst was pressed on the surface of silica/alumina tape using tungsten carbide press die, held inside a molybdenum alloy frame and treated by an e-beam heater to reach a specific temperature under ultra-high vacuum. For *in situ* heating procedure, the sample was first heated to 750 °C from room temperature with a ramping rate of $10 \text{ }^\circ\text{C min}^{-1}$, held at 150 °C, 250 °C, 350 °C, 450 °C, 550 °C, 650 °C and 750 °C respectively for the measurements of the survey (160 eV pass energy), C 1s

and N 1s (20 eV pass energy) spectra. It was then heated to 950 °C without the control of the ramping rate, followed by an immediate natural cooling down to 150 °C, and finally held at 150 °C. Similar spectra measurements were performed when the temperature reached 950 °C and was held at 150 °C respectively. For *in situ* double heating procedure, the sample was heated from 150 °C to 750 °C with a ramping rate of 10 °C min⁻¹, heated from 750 °C to 950 °C without ramping control, naturally cooled down to 150 °C and held at 150 °C in sequence. Then it repeated the same procedure once and was finally held at 150 °C. The spectra measurements were only performed at three 150 °C points (initial, first cooled and second cooled). Three independent measurements (*i.e.* a freshly prepared sample for every experiment) were performed for each analysis without the assistance of a charge neutralizer. CasaXPS software was utilized to analyze the data, using a 70% Gaussian / 30% Lorentzian line shape for curve fitting and linear background for quantifying atomic composition (Shirley background for Fe 2p). The corresponding peak position, range and full-width-at-half-maximum parameters in high resolution C 1s and N 1s spectra were fitted according to the previous publications[22,23,35,41,43,47].

Scanning Transmission Electron Microscopy Characterization. Aberration-corrected STEM was performed on a JEOL JEM-ARM300F microscope. High angle annular dark field (HAADF) (Z-contrast) images were recorded using a convergence semi-angle of 22 mrad, inner collection angle of 83 mrad and outer collection angle of 165 mrad respectively. For *in situ* heating STEM, the sample was heated to each specific temperature for imaging recording from room temperature to 950 °C and cooled down without ramping control under ultra-high vacuum. Energy dispersive X-ray spectroscopy (EDS) maps were only recorded before and after heating.

STEM-EELS was performed on a Nion UltraSTEM 200 HERMES microscope with a high-energy resolution monochromated electron energy loss spectroscopy (EELS) system. The equipment was operated at the accelerating voltage of 60 kV. The sample was vacuum heated at 160 °C to get rid of the contamination before putting into the microscope. For imaging, the convergence semi-angle was 33 mrad with a beam current of ~100pA. For spectroscopy, the EELS dispersion and dwell time were 0.4 eV/channel and 0.2 s/pixel, respectively. The background subtraction process for core-loss EELS was carried out by fitting a power-law function in the commercial software package Digital Micrograph. All reported temperatures were calculated by the measured electrical resistance of the heater. For the *in situ* heating experiment under a vacuum environment, images were taken at the pristine state, 650 °C, one area at 950 °C, and the final state after cool down. EELS spectra were collected when the images were taken. The

Protochips Fusion was used with the heating chip (E-FHDC, Protochips, Inc.). The threshold was done with the Image Processing Toolbox in Dragonfly 4.1.

Other Physical Characterization. X-ray diffraction (XRD) was performed on a Rigaku SmartLab X-ray diffractometer using a Cu K α source, equipped with an Anton Paar air-cooling heating module. The catalyst was pressed on a silica/alumina tape, held on AlN basement and covered by a graphite dome. Nitrogen gas was filled inside the dome while air blows on the dome surface to cool it down. For in situ heating XRD, two samples were heated from room temperature to 950 °C and held at 150 °C, 250 °C, 350 °C, 450 °C, 550 °C, 650 °C, 750 °C, 850 °C, 950 °C for fast pattern measurements with 2θ from 10° to 90° and high-resolution scanning with 2θ from 20° to 35° respectively. They were then naturally cooled down to 150 °C and held at this point for final measurements.

X-ray computed tomography (CT) was performed at Beamline 8.3.2 at Advanced Light Source at Lawrence Berkeley National Laboratory. White radiation was used to yield a voxel resolution of 1.3 μm . The image acquisition was accomplished with a 50 μm LuAg scintillator, a 5x lens, and an sCMOS PCO Edge camera. The catalyst was mounted on the top of a ceramic holder, which is placed inside a quartz tube. The tube was installed onto a rotation stage and went through a furnace. The top of the holder with the catalyst was located inside the furnace. N₂ was purged inside the quartz tube and continued flowing at 100 standard cubic centimeters per minute during the whole scanning process. For each scan, 1313 images were collected with an exposure time of 100 ms per image while the sample was rotated through 180 degrees. For in situ heating X-ray CT, the sample was heated from room temperature to 950 °C with 10 °C per minute, and held at 150 °C, 250 °C, 350 °C, 450 °C, 550 °C, 650 °C, 750 °C, 850 °C, 950 °C for a scanning. Three scans were accomplished at the point of 950 °C. The sample was then naturally cooled down to room temperature and held at this point for final measurement. The image stacks obtained from the first and last scans were segmented by Trainable Weka Segmentation, a machine learning analysis tool. A median filter was used to process the segmented result of the last scan images to decrease the impact of image noise. Dragonfly 4.1 was used to create the three-dimensional structures.

Nitrogen physisorption was performed in a Micromeritics 3Flex Surface and Catalyst Analyzer. The samples were vacuumed for 7h before the measurement (vacuum at 90 °C for 1h and then at 200 °C for 6h). The surface area was calculated by the Barrett-Emmett-Teller (BET) method. The pore size distribution was obtained with the non-local density function theory model (NLDFT).

Acknowledgements

IVZ and YH would like to acknowledge support from the National Science Foundation under CBET Award 1605159. XRD, TEM and nitrogen physisorption were performed at the UC Irvine Materials Research Institute (IMRI). XPS was performed at the UC Irvine Materials Research Institute (IMRI) using instrumentation funded in part by the National Science Foundation Major Research Instrumentation Program under grant no. CHE-1338173. The Advanced Light Source is supported by the Director, Office of Science, Office of Basic Energy Sciences, of the U.S. Department of Energy under Contract No. DE-AC02-05CH11231. We would like to thank Dr. Yuanchao Liu for the acquiring one of the BET data. We sincerely thank Dr. Dilworth Parkinson and Dr. Harold Barnard for Beamline 8.3.2 micro-CT support and for building a furnace set-up.

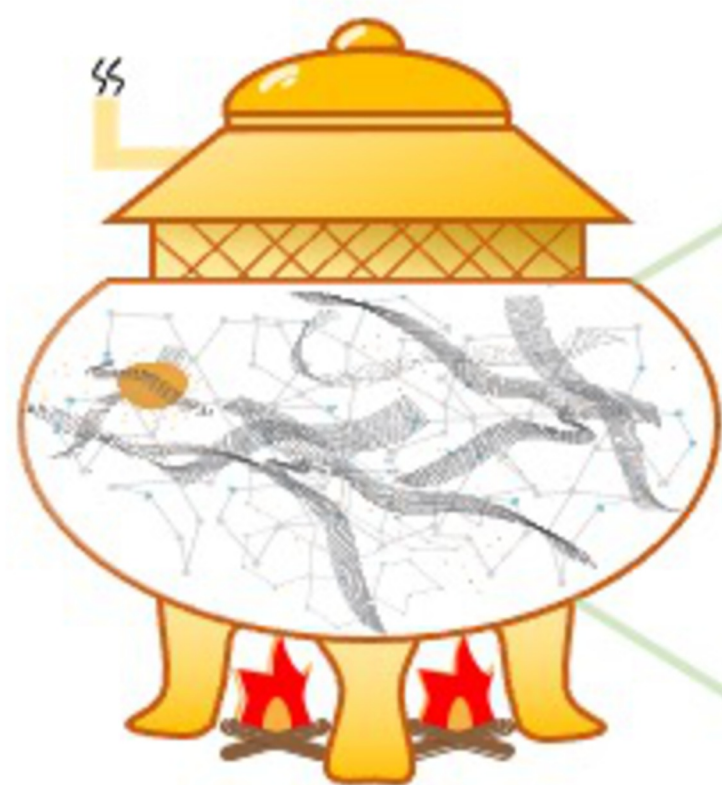
References

1. Thompson, S. T., *et al.*, *Solid State Ionics* (2018) **319**, 68, <https://doi.org/https://doi.org/10.1016/j.ssi.2018.01.030>
2. Shao, Y., *et al.*, *Advanced Materials* (2019) **31** (31), 1807615, <https://doi.org/10.1002/adma.201807615>
3. Collman, J. P., *et al.*, *Journal of the American Chemical Society* (1980) **102** (19), 6027, <https://doi.org/10.1021/ja00539a009>
4. Barkholtz, H. M., and Liu, D.-J., *Materials Horizons* (2017) **4** (1), 20, <https://doi.org/10.1039/C6MH00344C>
5. Varela, A. S., *et al.*, *ACS Catalysis* (2019) **9** (8), 7270, <https://doi.org/10.1021/acscatal.9b01405>
6. Qiao, J., *et al.*, *Chemical Society Reviews* (2014) **43** (2), 631, <https://doi.org/10.1039/C3CS60323G>
7. Asset, T., *et al.*, *ACS Catalysis* (2019) **9** (9), 7668, <https://doi.org/10.1021/acscatal.9b01513>
8. Mukherjee, S., *et al.*, *Nano Energy* (2018) **48**, 217, <https://doi.org/https://doi.org/10.1016/j.nanoen.2018.03.059>
9. Gao, Y., *et al.*, *ACS Applied Energy Materials* (2019) **2** (8), 6071, <https://doi.org/10.1021/acsaem.9b01135>
10. Foster, S. L., *et al.*, *Nature Catalysis* (2018) **1** (7), 490, <https://doi.org/10.1038/s41929-018-0092-7>
11. Asset, T., and Atanassov, P., *Joule* (2020) **4** (1), 33, <https://doi.org/https://doi.org/10.1016/j.joule.2019.12.002>

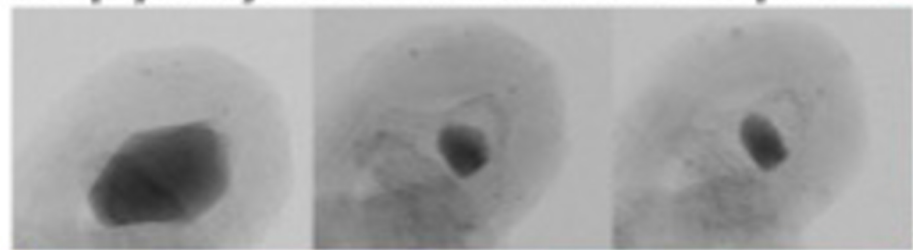
12. Sa, Y. J., *et al.*, *Journal of the American Chemical Society* (2016) **138** (45), 15046, <https://doi.org/10.1021/jacs.6b09470>
13. Karapinar, D., *et al.*, *Angewandte Chemie International Edition* (2019) **58** (42), 15098, <https://doi.org/10.1002/anie.201907994>
14. Li, J., *et al.*, *Journal of the American Chemical Society* (2019) <https://doi.org/10.1021/jacs.9b11197>
15. Pylypenko, S., *et al.*, *The Journal of Physical Chemistry C* (2011) **115** (28), 13667, <https://doi.org/10.1021/jp1122344>
16. Mamtani, K., *et al.*, *Catalysis Letters* (2016) **146** (9), 1749, <https://doi.org/10.1007/s10562-016-1800-z>
17. Ratsos, S., *et al.*, *Journal of Materials Chemistry A* (2018) **6** (30), 14663, <https://doi.org/10.1039/C8TA02325E>
18. Malko, D., *et al.*, *J Am Chem Soc* (2016) **138** (49), 16056, <https://doi.org/10.1021/jacs.6b09622>
19. Mamtani, K., *et al.*, *ACS Catalysis* (2016) **6** (10), 7249, <https://doi.org/10.1021/acscatal.6b01786>
20. Singh, D., *et al.*, *ACS Catalysis* (2014) **4** (10), 3454, <https://doi.org/10.1021/cs500612k>
21. Dong, K., *et al.*, *Angewandte Chemie* (2021) **133** (19), 10677, <https://doi.org/10.1002/anie.202101880>
22. Artyushkova, K., *et al.*, *Chemical Communications* (2013) **49** (25), 2539, <https://doi.org/10.1039/C3CC40324F>
23. Matanovic, I., *et al.*, *The Journal of Physical Chemistry C* (2016) **120** (51), 29225, <https://doi.org/10.1021/acs.jpcc.6b09778>
24. Zitolo, A., *et al.*, *Nature Communications* (2017) **8** (1), 957, <https://doi.org/10.1038/s41467-017-01100-7>
25. Primbs, M., *et al.*, *Energy & Environmental Science* (2020) **13** (8), 2480, <https://doi.org/10.1039/D0EE01013H>
26. Specchia, S., *et al.*, *Current Opinion in Electrochemistry* (2021), 100687, <https://doi.org/10.1016/j.coelec.2021.100687>
27. Kumar, K., *et al.*, *ACS Catalysis* (2020) **11** (2), 484, <https://doi.org/10.1021/acscatal.0c04625>
28. Li, J., *et al.*, *Nature Catalysis* (2021) **4** (1), 10, <https://doi.org/10.1038/s41929-020-00545-2>
29. Huang, Y., *et al.*, *Materials Today* (2021) **47**, 53, <https://doi.org/10.1016/j.mattod.2021.02.006>

30. Chung, H. T., *et al.*, *Science* (2017) **357** (6350), 479, <https://doi.org/10.1126/science.aan2255>
31. Strickland, K., *et al.*, *ACS Catalysis* (2018) **8** (5), 3833, <https://doi.org/10.1021/acscatal.8b00390>
32. Workman, M. J., *et al.*, *Journal of Power Sources* (2017) **348**, 30, <https://doi.org/10.1016/j.jpowsour.2017.02.067>
33. Yang, H.-J., *et al.*, *ChemSusChem* (2019) **12** (17), 3988, <https://doi.org/10.1002/cssc.201901330>
34. Türk, K. K., *et al.*, *International Journal of Hydrogen Energy* (2018) **43** (51), 23027, <https://doi.org/https://doi.org/10.1016/j.ijhydene.2018.10.143>
35. Artyushkova, K., *et al.*, *ACS Applied Energy Materials* (2019) **2** (8), 5406, <https://doi.org/10.1021/acsaem.9b00331>
36. Shard, A. G., *Surface and Interface Analysis* (2014) **46** (3), 175, <https://doi.org/10.1002/sia.5406>
37. Knipe, S. W., *et al.*, *Geochimica et Cosmochimica Acta* (1995) **59** (6), 1079, [https://doi.org/https://doi.org/10.1016/0016-7037\(95\)00025-U](https://doi.org/https://doi.org/10.1016/0016-7037(95)00025-U)
38. Yang, C., *et al.*, *ChemPhysChem* (2017) **18** (14), 1874, <https://doi.org/10.1002/cphc.201700240>
39. Seah, M. P., and Dench, W. A., *Surface and Interface Analysis* (1979) **1** (1), 2, <https://doi.org/10.1002/sia.740010103>
40. Jackson, S. T., and Nuzzo, R. G., *Applied Surface Science* (1995) **90** (2), 195, [https://doi.org/https://doi.org/10.1016/0169-4332\(95\)00079-8](https://doi.org/https://doi.org/10.1016/0169-4332(95)00079-8)
41. Artyushkova, K., *et al.*, *The Journal of Physical Chemistry C* (2015) **119** (46), 25917, <https://doi.org/10.1021/acs.jpcc.5b07653>
42. Fujimoto, A., *et al.*, *Analytical Chemistry* (2016) **88** (12), 6110, <https://doi.org/10.1021/acs.analchem.6b01327>
43. Matanovic, I., *et al.*, *Current Opinion in Electrochemistry* (2018) **9**, 137, <https://doi.org/https://doi.org/10.1016/j.coelec.2018.03.009>
44. Matter, P. H., *et al.*, *Journal of Catalysis* (2006) **239** (1), 83, <https://doi.org/https://doi.org/10.1016/j.jcat.2006.01.022>
45. Liu, J., *et al.*, *Carbon* (2017) **115**, 763, <https://doi.org/https://doi.org/10.1016/j.carbon.2017.01.080>
46. Zhao, Y., *et al.*, *Nature Chemistry* (2018) **10** (9), 924, <https://doi.org/10.1038/s41557-018-0100-1>
47. Chen, Y., *et al.*, *ACS Applied Energy Materials* (2018) **1** (11), 5948, <https://doi.org/10.1021/acsaem.8b00959>

48. Wu, G., *et al.*, *Science* (2011) **332** (6028), 443, <https://doi.org/10.1126/science.1200832>
49. Chung, H. T., *et al.*, *Nature Communications* (2013) **4** (1), 1922, <https://doi.org/10.1038/ncomms2944>
50. Wu, G., *et al.*, *Nano Energy* (2016) **29**, 83, <https://doi.org/https://doi.org/10.1016/j.nanoen.2015.12.032>
51. Li, J., *et al.*, *Catalysts* (2019) **9** (2), 144,
52. Möller, T., *et al.*, *Energy & Environmental Science* (2019) **12** (2), 640, <https://doi.org/10.1039/C8EE02662A>
53. Oezaslan, M., *et al.*, *Chemistry of Materials* (2011) **23** (8), 2159, <https://doi.org/10.1021/cm103661q>
54. Serov, A., *et al.*, *Advanced Energy Materials* (2014) **4** (10), 1301735, <https://doi.org/10.1002/aenm.201301735>



re-pyrolysis in inert atmosphere



150 °C

450 °C

750 °C

950 °C

Room Cool

